

Stellar Loci V: Photometric Metallicities of 27 Million FGK Stars based on *Gaia* Early Data Release 3

SHUAI XU ¹, HAIBO YUAN ¹, ZEXI NIU ^{2,3}, LIN YANG ⁴, TIMOTHY C. BEERS ⁵, AND YANG HUANG ⁶

¹*Department of Astronomy, Beijing Normal University No.19, Xijiekouwai St, Haidian District, Beijing, 100875, P.R.China*

²*National Astronomical Observatories, Chinese Academy of Sciences, 20A Datun Road, Chaoyang District, Beijing, China*

³*University of Chinese Academy of Sciences, 19A Yuquan Road, Shijingshan District, Beijing, China*

⁴*College of Artificial Intelligence, Beijing Normal University No.19, Xijiekouwai St, Haidian District, Beijing, 100875, P.R.China*

⁵*Department of Physics and JINA Center for the Evolution of the Elements (JINA-CEE), University of Notre Dame, Notre Dame, IN 46556, USA*

⁶*South-Western Institute for Astronomy Research, Yunnan University, Kunming 650500, People's Republic of China*

(Received October 18, 2021; Revised November 15, 2021; Accepted November 20, 2021)

ABSTRACT

We combine LAMOST DR7 spectroscopic data and *Gaia* EDR3 photometric data to construct high-quality giant ($0.7 < (BP - RP) < 1.4$) and dwarf ($0.5 < (BP - RP) < 1.5$) samples in the high Galactic latitude region, with precise corrections for magnitude-dependent systematic errors in the *Gaia* photometry and careful reddening corrections using empirically determined color- and reddening-dependent coefficients. We use the two samples to build metallicity-dependent stellar loci of *Gaia* colors for giants and dwarfs, respectively. For a given $(BP - RP)$ color, a one dex change in $[\text{Fe}/\text{H}]$ results in about a 5 mmag change in $(BP - G)$ color for solar-type stars. These relations are used to determine metallicity estimates from EDR3 colors. Despite the weak sensitivity, the exquisite data quality of these colors enables a typical precision of about $\delta [\text{Fe}/\text{H}] = 0.2$ dex. Our method is valid for FGK stars with $G \leq 16$, $[\text{Fe}/\text{H}] \geq -2.5$, and $E(B - V) \leq 0.5$. Stars with fainter G magnitudes, lower metallicities, or larger reddening suffer from higher metallicity uncertainties. With the enormous data volume of *Gaia*, we have measured metallicity estimates for about 27 million stars with $10 < G \leq 16$ across almost the entire sky, including over 6 million giants and 20 million dwarfs, which can be used for a number of studies. These include investigations of Galactic formation and evolution, the identification of candidate stars for subsequent high-resolution spectroscopic follow-up, the identification of wide binaries, and to obtain metallicity estimates of stars for asteroseismology and exoplanet research.

Keywords: stars: fundamental parameters stars:abundances methods: data analysis Galaxy: stellar content

1. INTRODUCTION

The abundance of metals (metallicity; often parametrized by $[\text{Fe}/\text{H}]$) is one of the most important stellar parameters, as the atmospheric metallicities of long-lived low-mass stars retain a fossil record of the chemical composition of the interstellar medium at the time and place of their formation. Thus, a census of stellar metallicity plays an important role in understanding the formation and evolution of the Galaxy. (e.g., Beers

& Christlieb 2005; Casagrande et al. 2011; Peng et al. 2013; Wright et al. 2021).

Up till now, stellar metallicities have been measured primarily from spectroscopic surveys, such as the Sloan Digital Sky Survey (SDSS; York et al. 2000; Yanny et al. 2009), the Radial Velocity Experiment (RAVE; Steinmetz et al. 2006), the Large Sky Area Multi-Object Fiber Spectroscopic Telescope (LAMOST; Luo et al. 2015), the Apache Point Observatory Galactic Evolution Experiment (APOGEE; Majewski et al. 2016), and the GALactic Archaeology with HERMES (GALAH; Buder et al. 2018) survey. This approach has advantages and disadvantages. It can, for example, achieve an accuracy

of 0.03 dex – 0.1 dex for individual elements from spectra with high signal-to-noise ratios ($S/N > 50$) (e.g., García Pérez et al. 2016; Xiang et al. 2019; Ahumada et al. 2020; Jönsson et al. 2020; Buder et al. 2021). However, spectroscopic observations and analysis are time-consuming compared to photometric studies. Spectroscopic surveys also potentially suffer from strong selection effects, compromising interpretations of the resulting metallicity distributions.

Stellar metallicities can be also obtained through an analysis of photometric data (e.g., Ivezić et al. 2008; Starkenburg et al. 2017; Casagrande et al. 2019; Huang et al. 2019, 2021b; Whitten et al. 2019, 2021; An & Beers 2020, 2021a,b; Bonifacio et al. 2021). Although stellar colors are mostly dependent on effective temperature, they are also influenced by the atmospheric composition, though to a much lesser extent. The metallicity dependence is stronger for bluer colors, because of the presence of a large number of metallic absorption lines in the blue wavelength range.

Using the re-calibrated SDSS/Stripe 82 photometry (Yuan et al. 2015d), Yuan et al. (2015a) investigated the metallicity dependence and intrinsic widths of the SDSS stellar loci. It was found that a 1 dex decrease in metallicity typically resulted in a 0.20/0.02 mag decrease in the $u - g/g - r$ colors and a 0.02/0.02 mag increase in the $r - i/i - z$ colors, respectively. The intrinsic widths of the SDSS stellar loci are at maximum a few mmag. By simultaneously fitting the intrinsic colors $u - g$, $g - r$, $r - i$, and $i - z$ from SDSS with those predicted by the metallicity-dependent stellar loci, Yuan et al. (2015b) measured metallicity estimates for a half million FGK stars in SDSS Stripe 82, with a typical precision of 0.1 dex. Very recently, Zhang et al. (2021) presented metallicity-dependent SDSS stellar color loci for red giant stars. Systematic differences between the metallicity-dependent stellar loci of red giants and main-sequence stars were found. They applied the same technique to measure metallicities for red giant stars in Stripe 82, and achieved a typical precision of 0.2 dex.

Gaia Early Data Release 3 (EDR3; Brown et al. 2021) has provided the best photometric data to date, obtaining colors of unprecedented mmag precision for more than one billion stars. Such a huge data volume and high data quality make it an ideal database to estimate photometric metallicities for enormous numbers of stars. Indeed, Huang et al. (2021b) have combined narrow-band photometry from the SkyMapper Southern Survey (SMSS; Wolf et al. 2018; Onken et al. 2019) with broad-band *Gaia* colors to obtain metallicity estimates for some 24 Million giant and dwarf

stars in the Southern Hemisphere (limited by the footprint of SMSS), and demonstrated that excellent results ($\delta [Fe/H] \sim 0.20 - 0.25$ dex) can be obtained for stars with metallicities as low as $[Fe/H] \sim -3.5$, due to the additional sensitivity to metallicity from use of the SMSS u - and v -band filters along with the *Gaia* data. Bonifacio et al. (2021) employed a similar approach, combining broad-band SDSS photometry with *Gaia* photometry and parallaxes to obtain estimates of metallicity for around 24 Million main-sequence turnoff stars, achieving somewhat lower precision, as expected.

In this work, we construct the metallicity-dependent stellar loci for *Gaia* colors *alone*, and investigate the photometric metallicity precision that can be estimated from these very broad-band colors. The paper is organized as follows. In Section 2, we describe our data and the methods employed. The results are presented and tested in Section 3. We apply this approach to the entire *Gaia* EDR3 data (subject to a number of color and latitude cuts), and obtain metallicities for over 27 million stars covering almost the entire sky in Section 4. Section 5 presents a summary as well as future perspectives.

2. DATA AND METHODOLOGY

In order to construct our training and test samples, we cross-match *Gaia* EDR3 and LAMOST Data Release 7 (DR7). LAMOST has accumulated more than 10 million low-resolution spectra ($R \approx 1800$) of varying quality. Stellar atmospheric parameters for millions of stars are derived by its stellar parameter pipeline (LASP; Wu et al. 2011; Luo et al. 2015), with a typical precision of 0.1 dex for spectra of sufficient quality and signal-to-noise. T. Beers (private communication) has refined estimates of the stellar metallicities for LAMOST stars with $[Fe/H] \leq -1.8$ by application of the non-SEGUE Stellar Parameter Pipeline (n-SSPP; Beers et al. 2014, 2017), which is based on a subset of the methods originally developed for the SEGUE Stellar Parameter Pipeline (SSPP; Lee et al. 2008a,b; Allende Prieto et al. 2008; Lee et al. 2011, 2013).

For *Gaia* photometry, despite its mmag-level precision, magnitude-dependent systematic errors in the magnitudes and colors have been found in its DR2 (e.g., Maíz Apellániz & Weiler 2018; Weiler 2018; Niu et al. 2021a) and EDR3. Using the spectroscopic information for about 0.7 million stars from LAMOST DR7, Niu et al. (2021b) have provided precise corrections to the *Gaia* EDR3 colors with a spectroscopy-based stellar color regression method, achieving an internal calibration precision of about 1 mmag for the colors $G - RP$ and $BP - RP$, respectively. These corrections are applied in this work. Note the correction of Niu et al. (2021b)

has taken into account the G magnitude corrections recommended by the *Gaia* team [Riello et al. \(2021\)](#). To match with the magnitude range of [Niu et al. \(2021b\)](#), the G magnitude of our data is restricted to between 9.5 and 17.5. For *Gaia* parallaxes, the official correction is applied to the reported EDR3 values, as validated by [Huang et al. \(2021a\)](#).

2.1. Reddening Corrections

Due to the very broad passbands of *Gaia*, reddening corrections must be carefully performed. The [Schlegel, Finkbeiner, & Davis \(1998, hereafter SFD\)](#) dust reddening map is used, along with empirical color- and reddening-dependent coefficients for $(BP - G)$ and $(BP - RP)$. [Niu et al. \(2021b\)](#) have estimated empirical temperature- and reddening-dependent reddening coefficients of $(BP - G)$ and $(BP - RP)$ with respect to the SFD map. These coefficients work well in most cases, but they require knowledge of effective temperature and are fitted independently. We also note that the errors of our method are more sensitive to their ratios. Therefore, we first repeat the work of [Niu et al. \(2021b\)](#) to estimate R_{BP-RP} , but as a function of $(BP - RP)_0$ and $E(B - V)$. Then we fit R_{BP-G}/R_{BP-RP} to obtain R_{BP-G} . Here stellar reddening values of $E(BP - RP)$ and $E(BP - G)$ are derived using the star-pair technique (e.g., [Yuan et al. 2013, Ruoyi & Haibo 2020](#)). Note that the SFD map over-estimates reddening by about 14 per cent (e.g., [Arce & Goodman, Schlafly & Finkbeiner 2011, Yuan et al. 2013](#)); these systematic errors in the SFD map are naturally taken into account by our empirical coefficients. The results are as follows:

$$R_{BP-RP} = 1.6876 - 0.5327X - 1.0268Y + 0.2238X^2 + 0.0933XY + 0.7177Y^2 \quad (1)$$

$$R_{BP-RP}/R_{BP-G} = 2.9302 - 1.3140X - 0.3999Y + 0.3150X^2 + 0.2114XY - 0.1223Y^2, \quad (2)$$

where X is $(BP - RP)_0$, and Y is $E(B - V)$ from the SFD map. The fit result for R_{BP-RP}/R_{BP-G} is shown in the top panel of [Figure 1](#). The fitting residuals, as a function of $(BP - RP)$ and $E(B - V)$, are shown in the middle and bottom panels of [Figure 1](#), respectively. The trends of our coefficients with color are consistent with the color-dependent coefficients of [Casagrande et al. \(2021\)](#). Note that, in the above reddening coefficients, $(BP - RP)$ refers to intrinsic colors; iterations

are needed when using the coefficients. All colors referred to hereafter are the intrinsic (de-reddened) colors unless otherwise noted. For the G -band extinction coefficient, a constant value of 2.50 ([Chen et al. 2019](#)) is simply adopted, as extinction-corrected G magnitudes are only used for classifications of giants and dwarfs in this work.

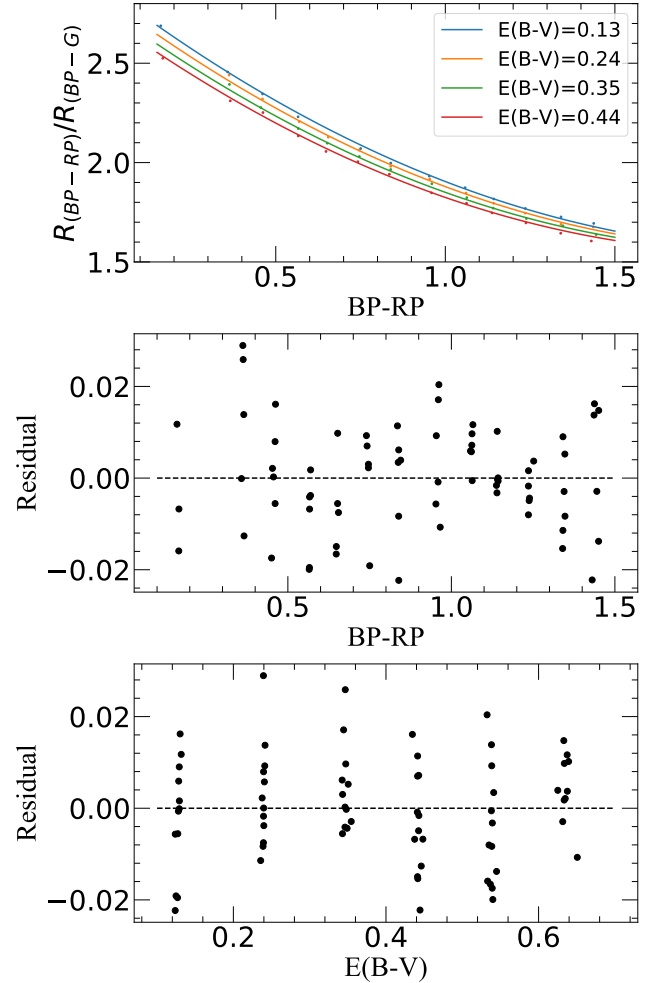


Figure 1. Top panel: R_{BP-RP}/R_{BP-G} , as a function of $(BP - RP)$, for different reddening values. The dots are empirically determined values; the lines are the fitting results. Middle and bottom panels: Fitting residuals, as a function of $(BP - RP)$ and $E(B - V)$, respectively. In these panels a dashed line is provided at the 0.00 residual level for reference.

2.2. Training Samples

We divide the sample into dwarfs and giants by an empirical cut, as shown by the red line in [Figure 2](#). The color range is set to be $0.7 < (BP - RP) < 1.5$ for the giants and $0.5 < (BP - RP) < 1.5$ for the dwarfs.

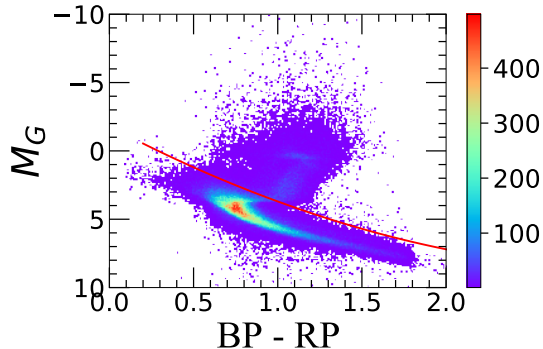


Figure 2. Color-magnitude diagram for the training sample. Colors indicate number densities, as shown in the color bar at right. Dwarfs and giants are separated by the red line: $M_G = -(BP - RP)^2 + 6.5 \times (BP - RP) - 1.8$.

First, we choose the LAMOST stellar spectra with signal-to-noise ratios in the g band (S/N_g) greater than 20 in order to obtain more reliable spectroscopic information. A cut of $|b| > 20^\circ$ is used to avoid high extinction in the low Galactic latitude region. We further exclude sources whose BP errors are larger than the median of BP errors for a given magnitude bin. Stars having G magnitudes from 12 to 14 have the best quality (Brown et al. 2021). This cut is applied for most stars in our training sample. However, for dwarf stars with lower metallicity ($[Fe/H] < -0.8$), we extend the faint limit to $G = 16$ to include a sufficient number of metal-poor dwarf stars.

The BP and RP magnitudes may suffer background and contamination issues, since they are obtained from aperture photometry. *Gaia* provides a `phot_bp_rp_excess_factor` parameter defined as $C = (I_{BP} + I_{RP})/I_G$ to evaluate this situation. As mentioned above, this excess factor suffers magnitude-dependent systematic errors as well. Yang et al. (2021) have made corrections for *Gaia* magnitudes using approximately 10,000 Landolt standard stars with a machine learning method. The systematic errors in the excess factor are essentially eliminated by applying their results. The excess factor is plotted against $(BP - RP)$ and colored by $[Fe/H]$ in the top panel of Figure 3. It can be seen that the excess factor also depends on $[Fe/H]$ for a given $(BP - RP)$. A 2nd-order two-dimensional polynomial is adopted to fit the relation among the excess factor, $(BP - RP)$, and $[Fe/H]$. We use a Gaussian profile to fit the distribution of residuals and obtain a dispersion, σ . Sources that run the risk of lower accuracy are dropped through a 3σ -clipping process, as shown in Figure 3. Finally, we obtain 35,164 giants and 195,155 dwarfs as our training samples. Their distributions in colors and magnitudes are shown in Figure 4.

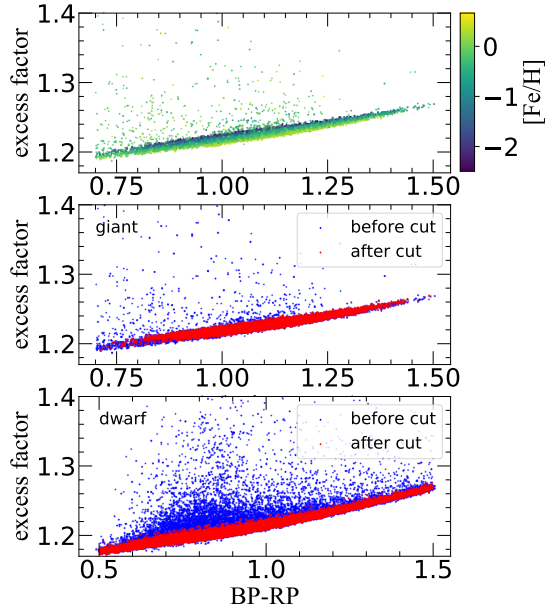


Figure 3. The `phot_bp_rp_excess_factor` as a function of $(BP - RP)$. Colors in the top panel indicates $[Fe/H]$ values, as shown in the color bar at right. The middle and bottom panels show before (blue dots) and after (red dots) comparisons as the result of the 3σ -clipping for giants and dwarfs, respectively.

2.3. Test Samples

As was the case for the training samples, in the assembly of our test samples we require stars with LAMOST spectra having S/N_g greater than 20. Another cut, which requires stars to have distance from the Galactic plane larger than 200 pc is applied, rather than $|b| > 20^\circ$. In addition, the `phot_bp_rp_excess_factor` is required to be $> 0.09 \times (BP - RP) + 1.15$, in order to excise potentially very inaccurate data. Note this criterion is much stricter than the one suggested by the *Gaia* team (Gaia Collaboration et al. 2021). The test samples contains 708,268 giants and 2,081,870 dwarfs. Their distributions in colors and magnitudes are shown in Figure 5. Compared with the training samples, the test samples have larger photometric errors and cover wider magnitude and extinction ranges.

2.4. Metallicity-dependent Stellar Loci

As shown in Zhang et al. (2021), metallicity-dependent stellar loci may differ between giants and dwarfs. Therefore, we fit the relations among $(BP - G)$, $(BP - RP)$, and $[Fe/H]$ with a least-squares method separately for the giants and the dwarfs, respectively. A 2nd-order two-dimensional polynomial with 6 free parameters is adopted for giant stars. A 3σ -clipping procedure is performed to reject outliers when fitting the data. The relation for giant stars is:

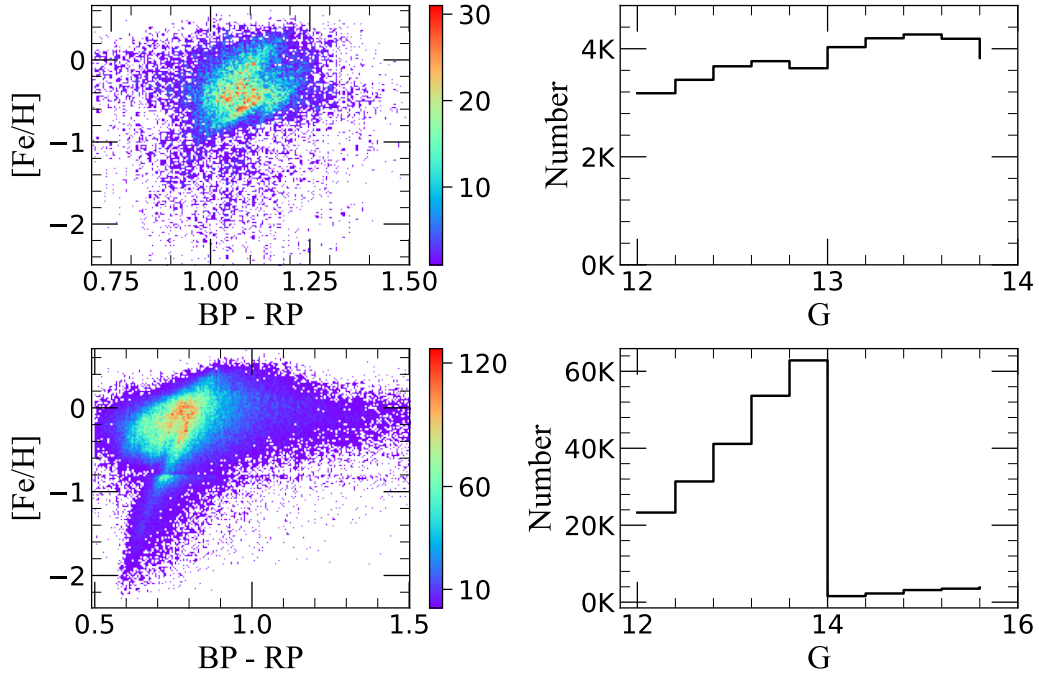


Figure 4. Left panels: Distributions of the giant (top) and dwarf (bottom) training samples in the $[\text{Fe}/\text{H}]$ vs. $(BP - RP)$ plane. The colors indicate the number densities, as shown in the color bar at right. Right panels: G magnitude distributions of the giant (top) and dwarf (bottom) training samples. Note that the stars of $14 < G < 16$ in the bottom-right panel are metal-poor dwarfs ($[\text{Fe}/\text{H}] < -0.8$)

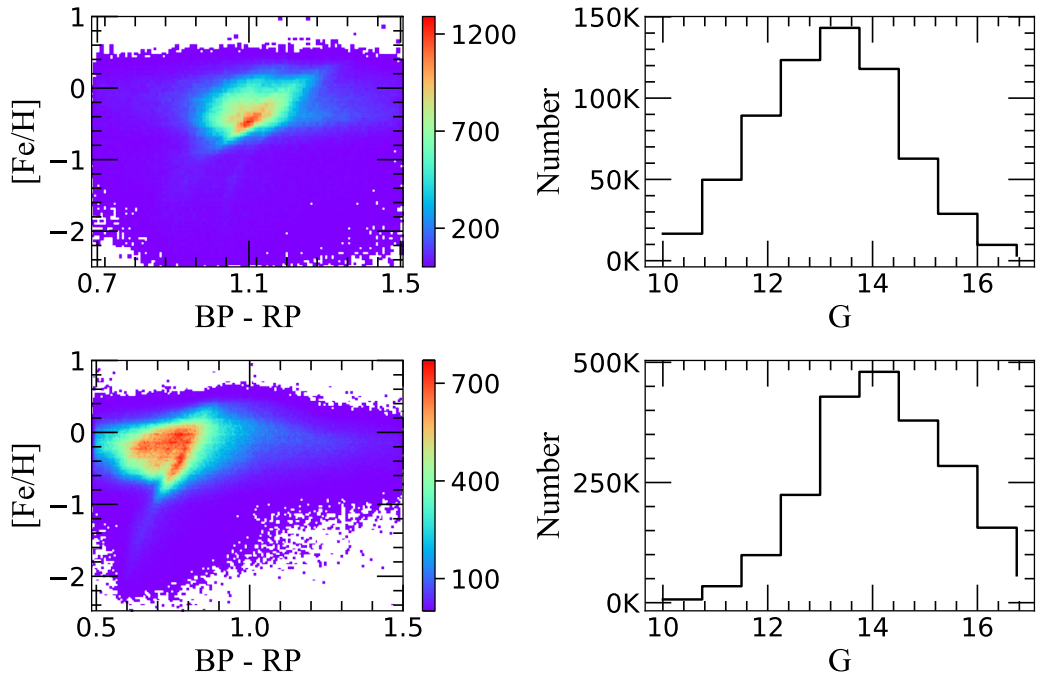


Figure 5. Same plot as Figure 4, but for the test samples.

$$(BP - G) = -6.402 \times 10^{-3} + 3.352 \times 10^{-1}X + 8.756 \times 10^{-3}Y + 8.975 \times 10^{-2}X^2 - 3.182 \times 10^{-3}XY + 9.230 \times 10^{-4}Y^2, \quad (3)$$

where X is the $(BP - RP)$ color and Y is $[\text{Fe}/\text{H}]$. The fitting residuals, as a function of $(BP - RP)$ and $[\text{Fe}/\text{H}]$, are plotted in the top panels of Figure 6. We use a Gaussian profile to fit the distribution of residuals; a σ of only 0.84 mmag centered at 0.004 mmag is obtained, as shown in the bottom-left panel. The bottom-right panel shows variations of the relation at different metallicities, relative to the one at $[\text{Fe}/\text{H}] = 0.0$. It can be seen that a 1 dex change in metallicity results in about a 5 mmag change in $(BP - G)$ color. The sensitivity for metal-rich stars is stronger than that for metal-poor stars, and stronger for bluer stars, as expected.

Similarly, a 3rd-order two-dimensional polynomial with 10 free parameters is adopted for the metallicity-dependent stellar locus of dwarf stars. The relation is

$$(BP - G) = 1.172 \times 10^{-2} + 2.762 \times 10^{-1}X + 9.170 \times 10^{-4}Y + 1.533 \times 10^{-1}X^2 + 1.010 \times 10^{-2}XY + 6.410 \times 10^{-4}Y^2 - 2.248 \times 10^{-2}X^3 - 5.230 \times 10^{-3}X^2Y + 4.610 \times 10^{-4}XY^2 + 0.000Y^3, \quad (4)$$

where X and Y are the same as in Eqn. 3. The fitting results are shown in Figure 7. The σ value is 0.96 mmag, slightly larger than that for giants. The tendency of metallicity sensitivity is the same as above, stronger for metal-rich stars than for metal-poor stars, and stronger for F/G/K stars than for A/M stars. Note that, due to the presence of unresolved dwarf-dwarf binaries, the distribution of the fitting residuals is asymmetric. Such features have been used previously to study binary fractions of dwarf stars (see, e.g., Yuan et al. 2015c; Niu et al. 2021).

3. RESULTS

In this section, we apply the above relations to estimate photometric metallicities from *Gaia* EDR3 colors. The $[\text{Fe}/\text{H}]$ calculated by our model is referred to below as $[\text{Fe}/\text{H}]_{\text{Gaia}}$. We define residuals $\Delta[\text{Fe}/\text{H}] = [\text{Fe}/\text{H}]_{\text{Gaia}} - [\text{Fe}/\text{H}]_{\text{LAMOST}}$ to evaluate the results.

3.1. Results for the Training Samples

We plot the photometric metallicities of the giant and dwarf training samples in Figure 8 and Figure 9, respectively. The histogram distributions of $\Delta[\text{Fe}/\text{H}]$ are

displayed in the top-left panels. The top-right panels plot the $[\text{Fe}/\text{H}]_{\text{Gaia}}$ vs. $[\text{Fe}/\text{H}]_{\text{LAMOST}}$. The bottom panels plot $\Delta[\text{Fe}/\text{H}]$ as a function of $(BP - RP)$ and $[\text{Fe}/\text{H}]_{\text{LAMOST}}$. Both giants and dwarfs exhibit reasonably good results, with a typical error of 0.18 dex. The median residuals are very close to zero. The differences exhibit little variation with $(BP - RP)$, but increase for more metal-poor stars, especially when $[\text{Fe}/\text{H}]_{\text{LAMOST}} < -1.5$, as expected.

3.2. Results for the Test Samples

We use the same methods as above in order to obtain the photometric $[\text{Fe}/\text{H}]$ estimates for the test samples. The results are plotted in Figures 10 and 11. As shown in the top-left panels, the standard deviations are 0.25 dex for the giants and 0.27 dex for the dwarfs, somewhat larger than those for the training samples, due primarily to the larger photometric errors in the test samples. The mean offsets are negative, -0.07 dex for giants and -0.09 dex for dwarfs, probably due to the effect of photometric errors. Since there are more metal rich than metal poor stars, errors will scatter more metal rich stars into the metal poor loci than vice versa. In the top-right panels, there are some outliers on the bottom right. We define these sources with $[\text{Fe}/\text{H}]_{\text{Gaia}} - [\text{Fe}/\text{H}]_{\text{LAMOST}} < -1$ dex as outliers, making up 2.1% of the giant test sample and 4.1% of the dwarf test sample. As shown in Figure 12, for the giants, the outliers have a larger phot_bp_rp_excess_factor and fainter G magnitudes, so naturally have larger errors. For the dwarfs, there are obviously more outliers due to unresolved binaries, which barely affect the giant stars (Niu et al. 2021), in addition to the two above reasons.

Because the test samples cover wider ranges of G magnitudes and extinctions comparing with the training samples, we consider their impact on the $[\text{Fe}/\text{H}]$ residuals. The middle and bottom panels of Figures 10 and 11 display, in turn, $\Delta[\text{Fe}/\text{H}]$ as a function of $(BP - RP)$, $[\text{Fe}/\text{H}]_{\text{LAMOST}}$, $E(B - V)$, and G magnitude. For the giants, one can see that the errors hardly change with the color. The errors increase slowly with reddening. The errors are larger for more metal-poor stars as found for the training sample. However, a systematic deviation gradually happens for $[\text{Fe}/\text{H}]_{\text{LAMOST}} < -2$. This arises because we do not have enough stars with $[\text{Fe}/\text{H}]_{\text{LAMOST}} < -2$ in the training sample, as seen in Figure 4. A small problem in Niu et al. (2021b) was also found from this analysis. These authors ignored the color dependency of the calibrations for stars of $G < 11.5$ mag because it is very weak (less than a few mmag). But in this work, even an error of 1 mmag

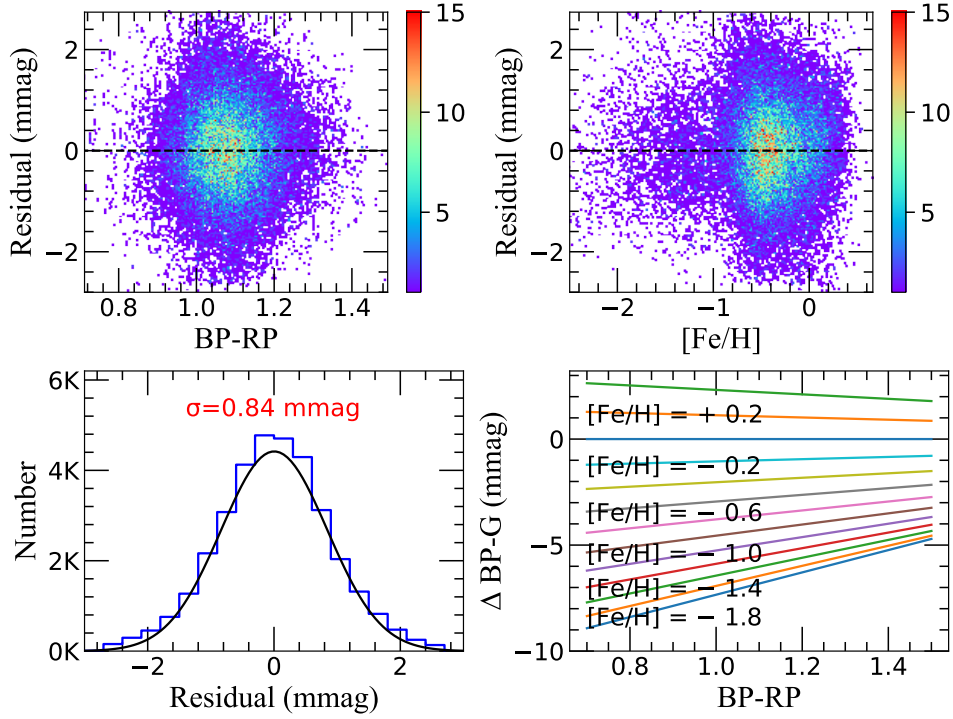


Figure 6. Top panels: Fitting residuals, as a function of $(BP - RP)$ color (left) and $[Fe/H]$ (right), for the giant training sample. The colors indicate the number densities, as shown in the color bar at right. In these panels a dashed line is provided at the 0.00 residual level for reference. Bottom left: Histogram distributions of the fitting residuals, with the Gaussian fitting profile over-plotted in black. Bottom right: Variations of stellar loci for different metallicities, relative to the one at $[Fe/H] = 0.0$.

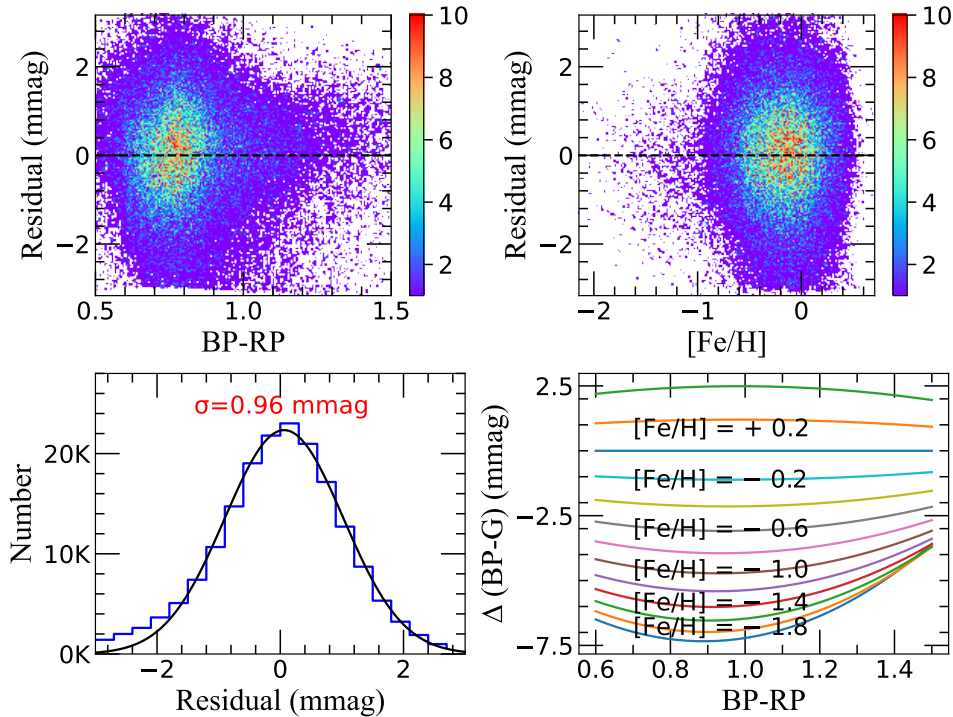


Figure 7. Same as Figure 6, but for the dwarf training sample.

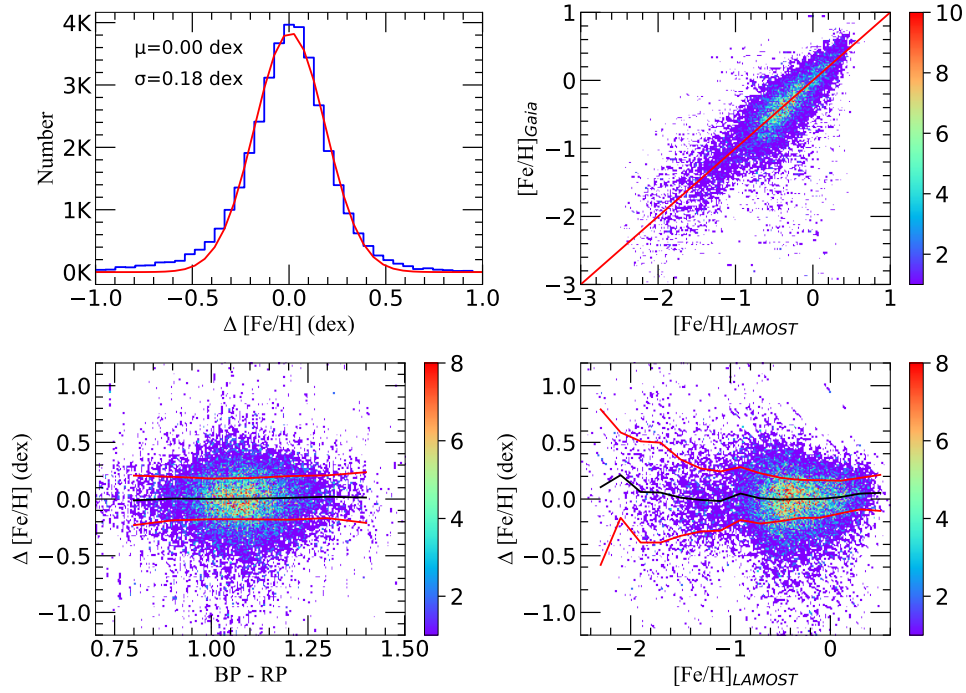


Figure 8. Results for the giant training sample. Top left: Histogram of the metallicity differences between those estimated from *Gaia* photometry and LAMOST spectroscopy. Gaussian fitting is over-plotted in red; the mean and sigma values are marked. Top right: *Gaia* metallicities vs. LAMOST metallicities. The red line is the one-to-one line. Bottom panels: Metallicity differences, as a function of $(BP - RP)$ color (left) and $[\text{Fe}/\text{H}]_{\text{LAMOST}}$ (right). The black lines indicate the medians; red lines indicate the standard deviations.

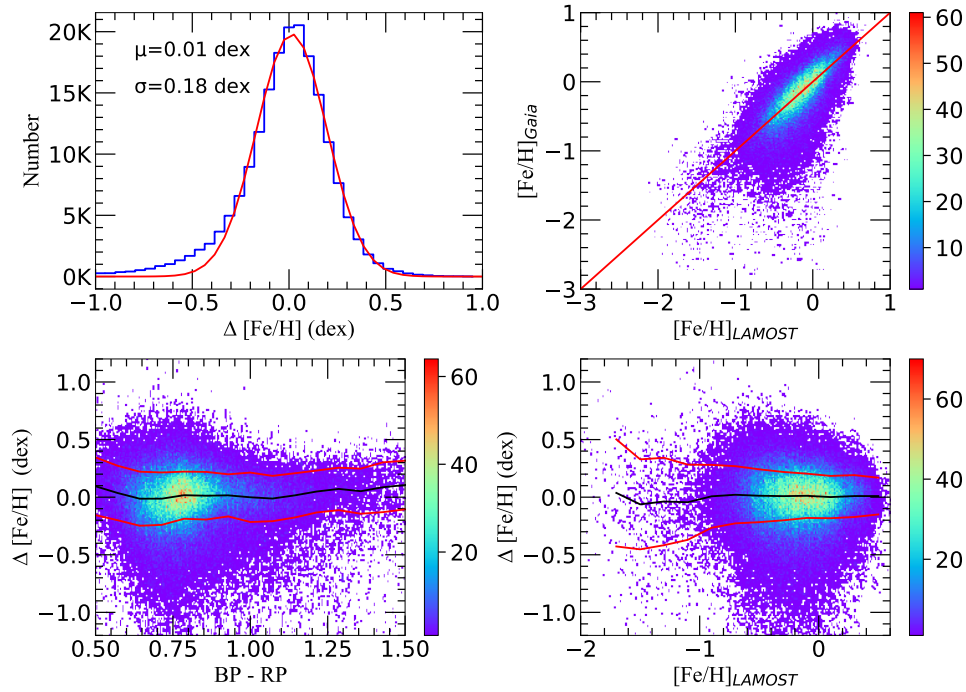


Figure 9. Same as Figure 8, but for the dwarf training sample. Note that in the top-left panel, the excess on the left side is due to the presence of dwarf-dwarf binary stars.

could affect the results. As a consequence, a magnitude-dependent systematic error exists in our model. We provide correction factors for application of our model for giants in the range $10 < G < 11.5$ in Table 1. This table lists the empirical offsets in metallicity, which are to be subtracted from the predicted $[\text{Fe}/\text{H}]$ of our model for the brighter stars. The results for the dwarfs are similar. A systematic deviation occurs for stars with $[\text{Fe}/\text{H}]_{\text{LAMOST}} < -1.7$ for similar reasons. A systematic deviation up to 0.3 dex is also noted for stars with $(BP - RP) > 1.2$.

There are no stars with $[\text{Fe}/\text{H}] < -2.5$ in the LAMOST DR7 data set due to the limitations of the LASP pipeline. To further test the limits of our method, we use metallicity estimates for LAMOST stars with $[\text{Fe}/\text{H}] \leq -1.8$ using the n-SSPP, as described above, which are valid down to $[\text{Fe}/\text{H}]$ about -4.0 . Problematic stars were rejected after visual inspection (by Beers). Only stars with $G \leq 16$ and spectra with $S/N_g > 20$ are used. The test results show that it is very challenging to reach below -2.5 with *Gaia* EDR3 colors alone.

Table 1. $[\text{Fe}/\text{H}]_{\text{Gaia}}$ Correction Factors for Giants with $10 < G < 11.5$.

G	$\Delta[\text{Fe}/\text{H}]$ (dex)	G	$\Delta[\text{Fe}/\text{H}]$ (dex)	G	$\Delta[\text{Fe}/\text{H}]$ (dex)
10.00	+0.385	10.50	+0.202	11.00	+0.101
10.05	+0.296	10.55	+0.289	11.05	+0.080
10.10	+0.406	10.60	+0.330	11.10	+0.063
10.15	+0.378	10.65	+0.328	11.15	+0.064
10.20	+0.364	10.70	+0.372	11.20	-0.007
10.25	+0.321	10.75	+0.301	11.25	+0.048
10.30	+0.341	10.80	+0.260	11.30	+0.066
10.35	+0.179	10.85	+0.165	11.35	+0.082
10.40	+0.254	10.90	+0.094	11.40	+0.028
10.45	+0.273	10.95	+0.097	11.45	+0.038

3.3. An External Test with Open Clusters

Cantat-Gaudin et al. (2018) have compiled a list of thousands of known or putative open clusters and their member stars based on *Gaia* DR2. We cross-match their catalogs with our test samples and obtain 812 sources in 70 open clusters in common. NGC 2682, NGC 2281, and NGC 1245 are selected to test our model. The results are shown in Figure 13. We can see that our photometric metallicities are consistent with the LAMOST DR7 results, with the mean metallicity differences close to zero and the σ values in the range 0.11 to 0.26 dex. NGC 1245 has the smallest σ value because its member stars are relatively brighter. There are also a few metallicity outliers, as indicated by orange crosses in the first column

of panels. Their distributions in the color-magnitude and color-color diagrams suggest that they are binaries or are affected by nearby stars.

3.4. Loci Differences between Dwarfs and Giants

As mentioned above, metallicity-dependent stellar loci may be different between dwarfs and giants. We define $\Delta(BP - G) = (BP - G)_{\text{dwarf}} - (BP - G)_{\text{giant}}$ for a given $(BP - RP)$ and $[\text{Fe}/\text{H}]$. The effect of $(BP - RP)$ and $[\text{Fe}/\text{H}]$ on $\Delta(BP - G)$ is shown in Figure 14. At $[\text{Fe}/\text{H}] = 0$, the difference is almost 0 when $0.7 < BP - RP < 1.2$. For stars with $(BP - RP) > 1.0$, the effect on $[\text{Fe}/\text{H}]$ is small; the difference is almost completely dominated by $(BP - RP)$, and becomes larger for redder stars. For stars with $(BP - RP) < 1.0$, the difference is larger at lower metallicities and for bluer stars. The largest difference is about 2 mmag, suggesting that the largest error of our model could reach about 0.4 dex if a source is mistakenly classified.

4. THE FINAL SAMPLE

In this section, we apply our methods to the entire *Gaia* data set in the applicable range of magnitude and colors. We first select all stars of $10 < G \leq 16$ and $|b| > 10^\circ$. Then, after the same cuts on phot_bp_rp_excess_factor and $BP - RP$ color as for the test sample are made, along with a cut on reddening $E(B - V) \leq 0.5$, 6,600,648 giants and 20,404,437 dwarfs remain in the final sample. Their color-magnitude diagram is plotted in Figure 15.

Metallicities for stars in the final sample are derived with our method (taking into account the corrections for bright stars given in Table 1), and the errors in metallicities are also estimated based on the photometric errors. The median errors are 0.29 dex and 0.34 dex for giants and dwarfs, respectively. At $G = 14/15/16$, the typical errors are 0.22/0.35/0.61 dex for giants, and 0.21/0.34/0.58 dex for dwarfs, respectively.

The $[\text{Fe}/\text{H}]$ distributions are shown in Figure 16. For giants, there are 2.0, 15.7, 80.8, 19.2, and 2.0 per cent stars with $[\text{Fe}/\text{H}] \leq -2.0, \leq -1.0, \leq 0, > 0$, and $> +0.5$, respectively. For dwarfs, there are 1.1, 11.7, 73.3, 26.7, and 3.2 per cent stars with $[\text{Fe}/\text{H}] \leq -2.0, \leq -1.0, \leq 0, > 0$, and $> +0.5$, respectively.

The spatial distributions in the Z-R plane can be seen in Figure 17, where Z is the distance to the Galactic plane, and R is the Galactocentric distance. The giants and dwarfs are divided into different panels in the Z-R plane. Their median metallicities are plotted in Figure 18. The vertical metallicity gradients of the disk stars are clearly seen in both panels. The separation between disk stars and halo stars and the flaring of the Galactic disk are also clear in the left panel.

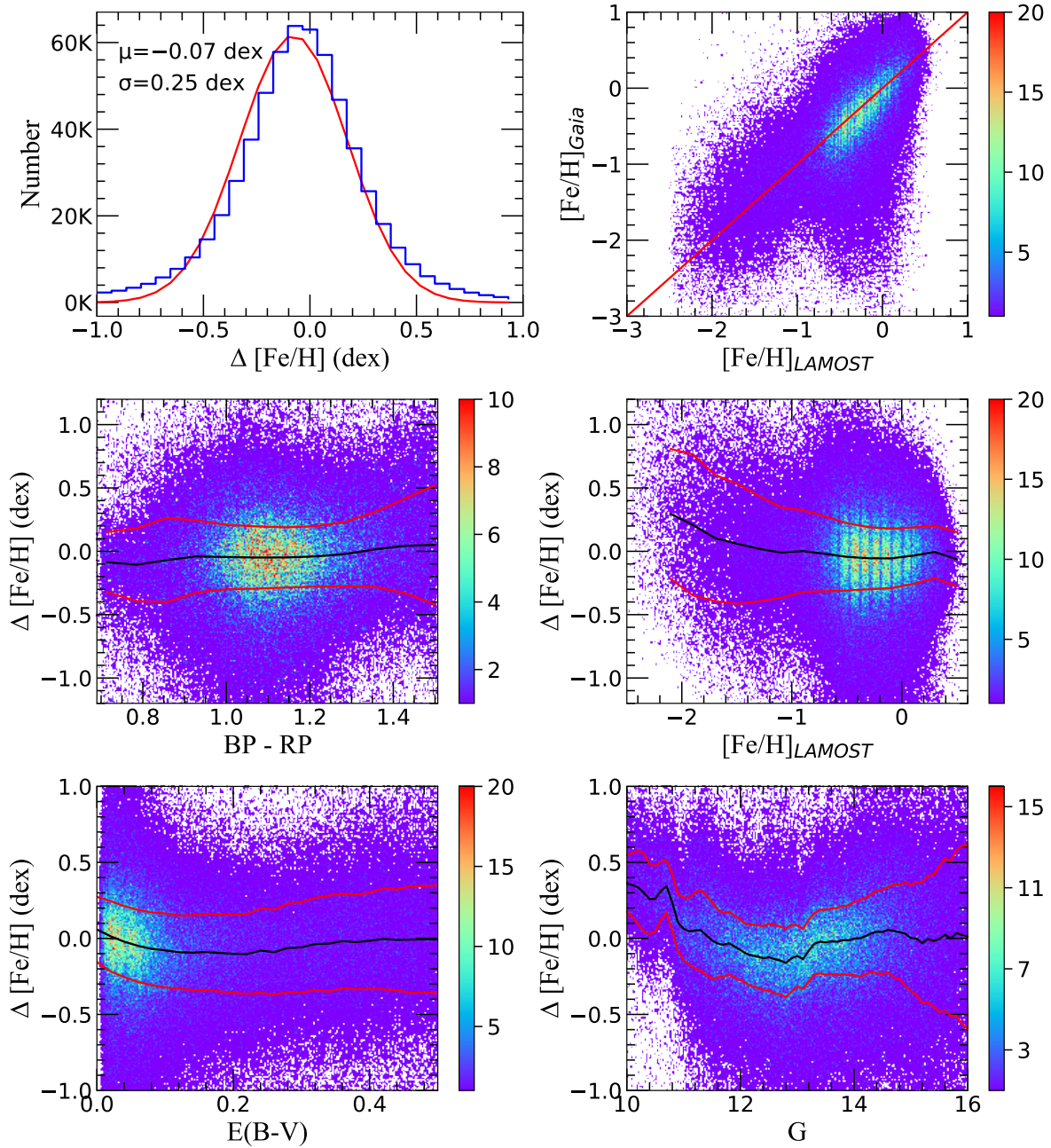


Figure 10. Results for the giant test sample. Top left: Histogram distribution of the metallicity differences that are respectively deduced from *Gaia* photometry and LAMOST spectroscopy. Gaussian fitting is over-plotted in red; the mean and sigma values are marked. Top right: LAMOST metallicities vs. *Gaia* metallicities. The red line is the one-to-one line. Middle panels: Metallicity differences, as a function of $(BP - RP)$ (left) and $[Fe/H]$ (right). Bottom panels: Metallicity differences, as a function of reddening (left) and G magnitude (right).

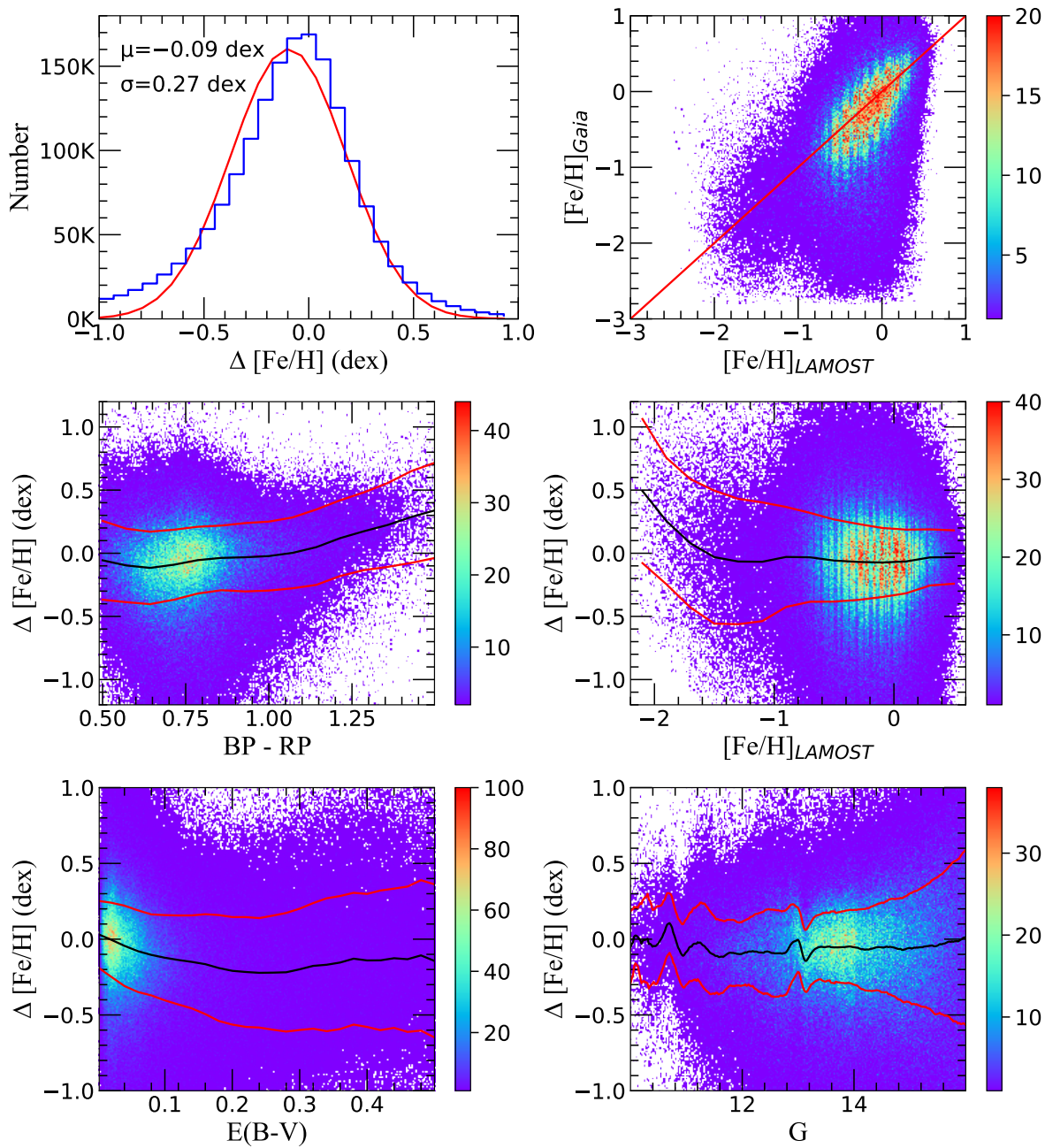


Figure 11. Same plot as Figure 10, but for the dwarf test sample.

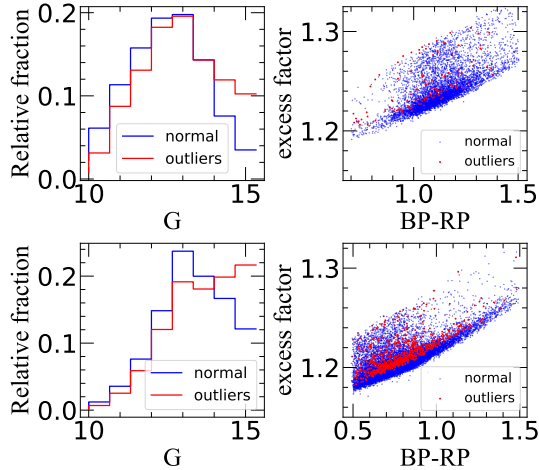


Figure 12. Analysis of the outliers. Top left: G magnitude distributions of the normal (blue line) and outliers (red line) for the giants. Top right: The `phot_bp_rp_excess_factor`, as a function of $(BP - RP)$, for the giants. Bottom: Same as the top panel, but for the dwarfs. To avoid crowding, only 1 per cent of randomly selected stars are plotted.

Table 2 lists the columns contained in the final sample catalog.

5. SUMMARY AND FUTURE PERSPECTIVES

In this work, we combine LAMOST DR7 spectroscopic data and *Gaia* EDR3 photometric data to assemble high-quality giant ($0.7 < (BP - RP) < 1.4$) and dwarf ($0.5 < (BP - RP) < 1.5$) samples in the high Galactic latitude region, with precise corrections for magnitude-dependent systematic errors in the *Gaia* photometry and careful reddening corrections using empirical color- and reddening-dependent coefficients. The two samples are used to construct metallicity-dependent stellar loci of *Gaia* colors for giants and dwarfs, respectively. For a given $(BP - RP)$ color, a one dex change in $[\text{Fe}/\text{H}]$ causes about a 5 mmag change in $(BP - G)$ color for solar-type stars. The metallicity-dependent loci are then used to determine stellar photometric metallicities from *Gaia* EDR3 colors. Owing to the exquisite data quality of *Gaia*, we have achieved a typical precision of about 0.2 dex for both giants and dwarfs, despite the very weak sensitivity of *Gaia* EDR3 colors on metallicity. Our tests show that the method is valid for FGK stars with $G \leq 16$, $[\text{Fe}/\text{H}] \geq -2.5$, and $E(B - V) \leq 0.5$. Stars with fainter G magnitudes, redder colors, lower metallicities, or larger reddening suffer from higher metallicity uncertainties. This work demonstrates the power of precision photometry in the determination of basic stellar parameters.

With the enormous data volume of *Gaia*, our method has measured metallicity estimates for about 27 million

bright stars with $10 < G \leq 16$ across almost the entire sky, including over 6 million giant stars and 20 million dwarfs. This is the largest catalog of metallicity estimates for stars to date, and should prove useful for a number of studies. For example, one can construct a magnitude-limited sample of red giants to study the structure and chemistry of the inner Galactic halo and the outer disk, or a magnitude-limited sample of FGK dwarfs with known metallicities to better investigate the star-formation history of the Solar Neighborhood using observed *Gaia* color-magnitude diagrams (e.g., Ruiz-Lara et al. 2020). The sample can also be used for the identification of candidate stars for subsequent high-resolution spectroscopic follow-up, or to select a pure sample of wide binaries (e.g., Ren et al. 2020; El-Badry et al. 2021) based on stars with common proper motions and similar metallicities, or obtain metallicities for a very large fraction of the TESS targets and investigate the occurrence rate of hot Jupiters for metal-poor stars (e.g., Boley et al. 2021). The catalog is publicly available via <https://doi.org/10.12149/101081>

Currently, our method uses the SFD reddening values to obtain metallicities from the *Gaia* colors. For nearby stars in the low Galactic latitude region, where the SFD map is not valid, three-dimensional reddening maps (e.g., Green et al. 2019; Chen et al. 2019) could be used instead, along with *Gaia* parallaxes. Alternatively, it is possible to derive reddening values and metallicities simultaneously, with help from infrared photometry obtained by 2MASS and WISE. Such explorations will be carried out in subsequent work. Obviously, applications of our approach to future releases from *Gaia*, will enable improved metallicity estimates and allow us to probe more distant stars.

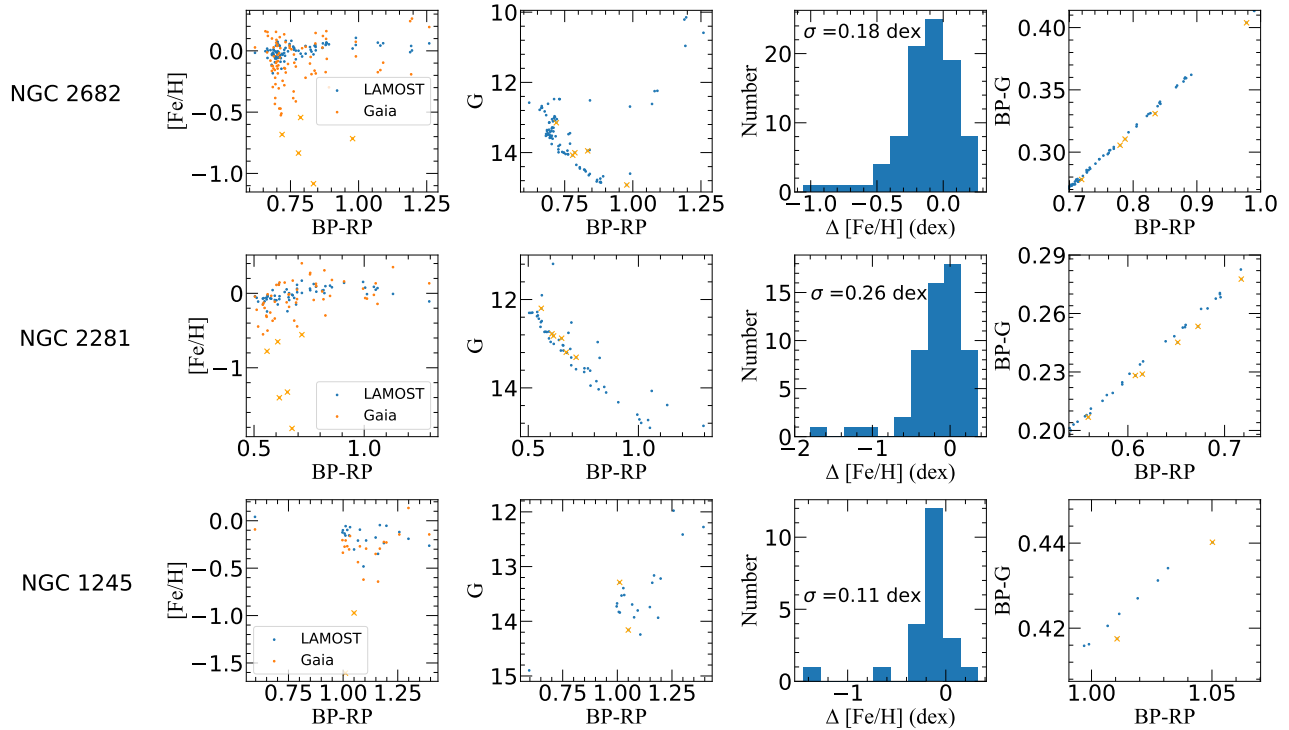


Figure 13. Test results for open clusters. The top, middle, and bottom panels are for NGC 2682, NGC 2281, and NGC 1245, respectively. For each cluster, the first column plots $[Fe/H]$ as a function of $(BP - RP)$. The blue and orange dots represent results from LAMOST DR7 and *Gaia* EDR3, respectively. The second column is the color-magnitude diagram. The third column is the histogram distribution of $\Delta[Fe/H]$ between the LAMOST DR7 and *Gaia* EDR3 results. The fourth column is the color-color diagram. The orange crosses in the second and fourth columns represent stars with large $\Delta[Fe/H]$ values.

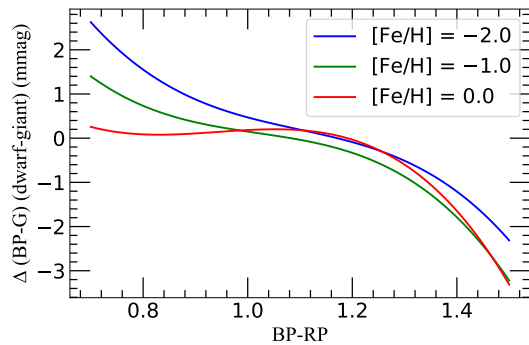


Figure 14. Differences in the loci between dwarfs and giants. The red, green, and blue lines correspond to three different metallicities.

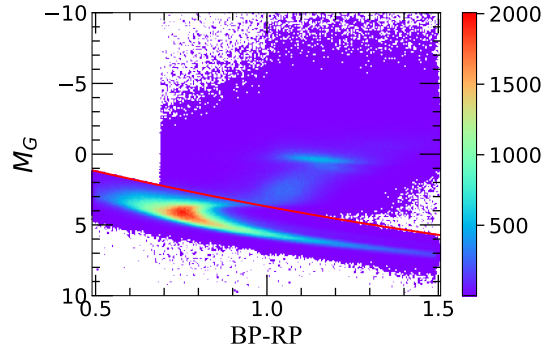


Figure 15. Color-magnitude diagram of the final sample. The colors indicate number densities, as shown in the color bar at right. Dwarfs and giants are separated by the red line: $M_G = -(BP - RP)^2 + 6.5 \times (BP - RP) - 1.8$.

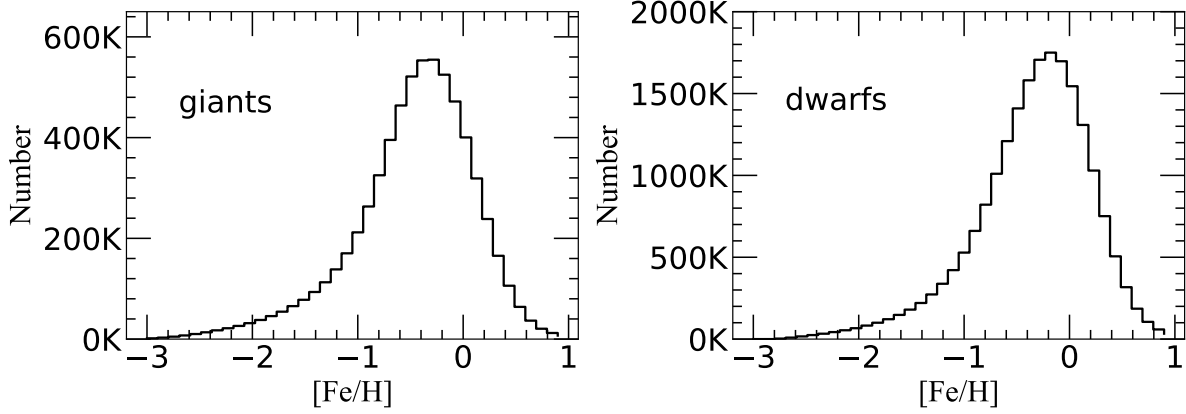


Figure 16. The $[\text{Fe}/\text{H}]$ distributions of the final sample. The left and right panels are for the giants and dwarfs, respectively.

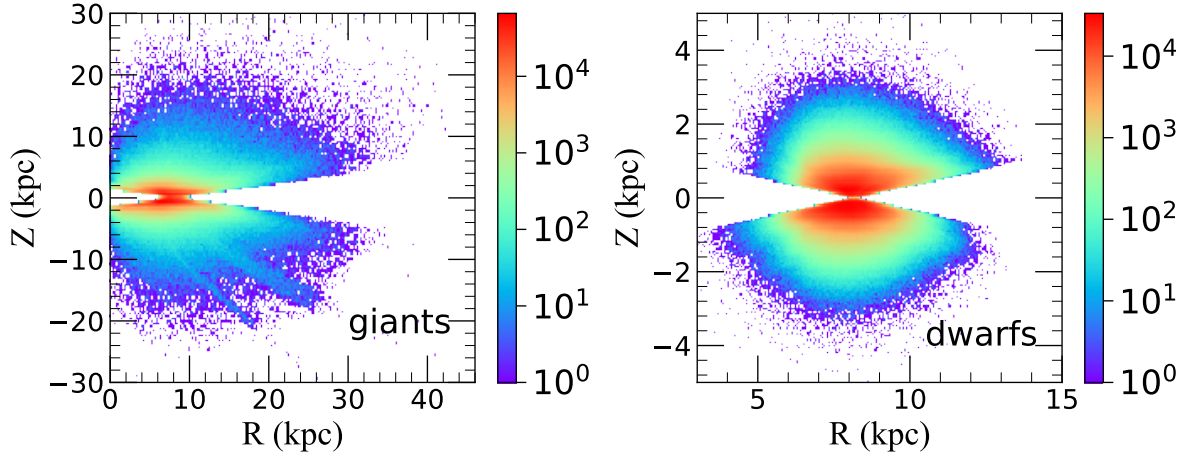


Figure 17. The spatial distributions in the Z - R plane of the final sample. The left and right panels are for the giants and dwarfs, respectively. The Sun is located at $(Z, R) = (0, 8.178)$ kpc. The colors indicate number densities, as shown in the color bars. Note that the two branches of stars visible in the lower right portion of the left panel are from the LMC and SMC.

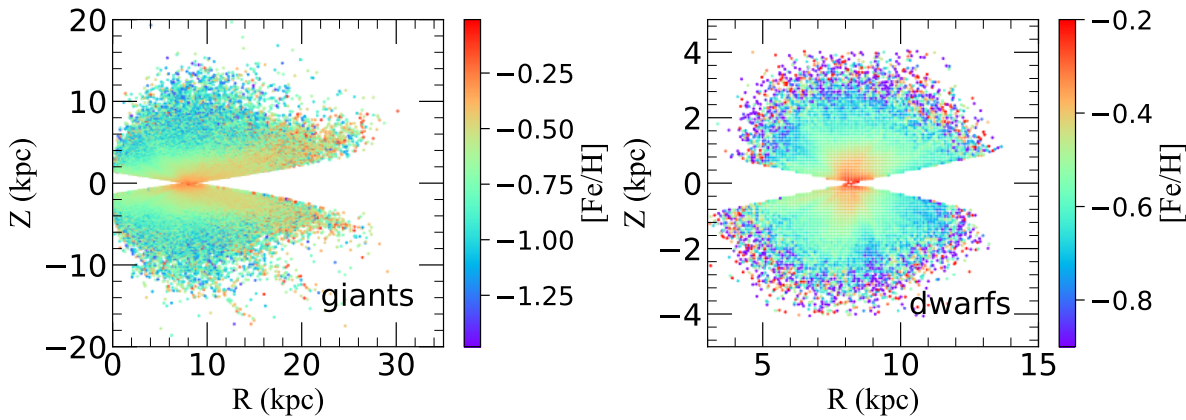


Figure 18. The spatial distributions in the Z - R plane of the final sample. The left and right panels are for the giants and dwarfs, respectively. The colors indicate $[\text{Fe}/\text{H}]$, as shown in the color bars. The Sun is located at $(Z, R) = (0, 8.178)$ kpc.

Table 2. Description of the Final Sample

Field	Description	Unit
source_id	Unique source identifier for EDR3 (unique with a particular Data Release)	–
ra	Right ascension	deg
dec	Declination	deg
parallax	Parallax	mas
parallax_error	Standard error of parallax	mas
pmra	Proper motion in right ascension direction	mas/year
pmra_error	Standard error of proper motion in right ascension direction	mas/year
pmdec	Proper motion in declination direction	mas/year
pmdec_error	Standard error of proper motion in declination direction	mas/year
ruwe	Renormalised unit weight error	–
phot_g_mean_flux_over_error	G-band mean flux divided by its error	–
phot_g_mean_mag	G-band mean magnitude	–
phot_bp_mean_flux_over_error	BP-band mean flux divided by its error	–
phot_bp_mean_mag	Integrated BP-band mean magnitude	–
phot_rp_mean_flux_over_error	RP-band mean flux divided by its error	–
phot_rp_mean_mag	Integrated RP-band mean magnitude	–
phot_bp_rp_excess_factor	BP/RP excess factor	–
l	Galactic longitude	deg
b	Galactic latitude	deg
ebv	Value of $E(B - V)$ from from the extinction map of SFD98	–
correct_bp_rp	Intrinsic $BP - RP$ color after color correction of Niu et al. (2021b)	–
correct_bp_g	Intrinsic $BP - G$ color after color correction of Niu et al. (2021b)	–
type	Flag to indicate classifications of stars; 0 for dwarfs and 1 for giants	–
correct_g_rp	Intrinsic $G - RP$ color after color correction of Niu et al. (2021b)	–
FeH_Gaia	Photometric metallicity	–
FeH_Gaia_error	Formal error of FeH_Gaia	dex
parallax_corrected	Parallax corrected by Lindegren et al. (2021)	mas

We acknowledge useful discussions with Dr. Xiaoting Fu. This work is supported by the National Natural Science Foundation of China through the projects NSFC 12173007, 11603002, 11933004, National Key Basic R & D Program of China via 2019YFA0405500, Beijing Normal University grant No. 310232102. T.C.B. acknowledges partial support from grant PHY 14-30152, Physics Frontier Center/JINA Center for the Evolution of the Elements (JINA-CEE), awarded by the US National Science Foundation. His participation in this work was initiated by conversations that took place during a visit to China in 2019, supported by a PIFI Distinguished Scientist award from the Chinese Academy of Science. We acknowledge the science research grants from the China Manned Space Project with NO. CMS-CSST-2021-A08 and CMS-CSST-2021-A09.

This work has made use of data from the European Space Agency (ESA) mission *Gaia* (<https://www.cosmos.esa.int/gaia>), processed by the Gaia Data Processing and Analysis Consortium (DPAC, <https://www.cosmos.esa.int/web/gaia/dpac/consortium>). Funding for the DPAC has been provided by national institutions, in particular the institutions participating in the Gaia Multilateral Agreement. Guoshoujing Telescope (the Large Sky Area Multi-Object Fiber Spectroscopic Telescope LAMOST) is a National Major Scientific Project built by the Chinese Academy of Sciences. Funding for the project has been provided by the National Development and Reform Commission. LAMOST is operated and managed by the National Astronomical Observatories, Chinese Academy of Sciences.

REFERENCES

- Ahumada, R., Prieto, C. A., Almeida, A., et al. 2020, *ApJS*, 249, 3, doi: [10.3847/1538-4365/ab929e](https://doi.org/10.3847/1538-4365/ab929e)
- Allende Prieto, C., Sivarani, T., Beers, T. C., et al. 2008, *AJ*, 136, 2070, doi: [10.1088/0004-6256/136/5/2070](https://doi.org/10.1088/0004-6256/136/5/2070)
- An, D., & Beers, T. C. 2020, *ApJ*, 897, 39, doi: [10.3847/1538-4357/ab8d39](https://doi.org/10.3847/1538-4357/ab8d39)
- . 2021a, *ApJ*, 907, 101, doi: [10.3847/1538-4357/abccd2](https://doi.org/10.3847/1538-4357/abccd2)
- . 2021b, *ApJ*, 918, 74, doi: [10.3847/1538-4357/ac07a4](https://doi.org/10.3847/1538-4357/ac07a4)
- Arce, H. G., & Goodman, A. A. 1999, *ApJL*, 512, L135, doi: [10.1086/311885](https://doi.org/10.1086/311885)
- Beers, T. C., & Christlieb, N. 2005, *Highlights of Astronomy*, 13, 579
- Beers, T. C., Norris, J. E., Placco, V. M., et al. 2014, *ApJ*, 794, 58, doi: [10.1088/0004-637X/794/1/58](https://doi.org/10.1088/0004-637X/794/1/58)
- Beers, T. C., Placco, V. M., Carollo, D., et al. 2017, *ApJ*, 835, 81, doi: [10.3847/1538-4357/835/1/81](https://doi.org/10.3847/1538-4357/835/1/81)
- Boley, K. M., Wang, J., Zinn, J. C., et al. 2021, *AJ*, 162, 85, doi: [10.3847/1538-3881/ac0e2d](https://doi.org/10.3847/1538-3881/ac0e2d)
- Bonifacio, P., Monaco, L., Salvadori, S., et al. 2021, *A&A*, 651, A79, doi: [10.1051/0004-6361/202140816](https://doi.org/10.1051/0004-6361/202140816)
- Brown, A. G. A., Vallenari, A., Prusti, T., et al. 2021, *Astronomy & Astrophysics*, 650, C3, doi: [10.1051/0004-6361/202039657e](https://doi.org/10.1051/0004-6361/202039657e)
- Buder, S., Asplund, M., Duong, L., et al. 2018, *Monthly Notices of the Royal Astronomical Society*, 478, 4513, doi: [10.1093/mnras/sty1281](https://doi.org/10.1093/mnras/sty1281)
- Buder, S., Sharma, S., Kos, J., et al. 2021, *MNRAS*, doi: [10.1093/mnras/stab1242](https://doi.org/10.1093/mnras/stab1242)
- Cantat-Gaudin, T., Jordi, C., Vallenari, A., et al. 2018, *A&A*, 618, A93, doi: [10.1051/0004-6361/201833476](https://doi.org/10.1051/0004-6361/201833476)
- Casagrande, L., Schönrich, R., Asplund, M., et al. 2011, *A&A*, 530, A138, doi: [10.1051/0004-6361/201016276](https://doi.org/10.1051/0004-6361/201016276)

- Casagrande, L., Wolf, C., Mackey, A. D., et al. 2019, *MNRAS*, 482, 2770, doi: [10.1093/mnras/sty2878](https://doi.org/10.1093/mnras/sty2878)
- Casagrande, L., Lin, J., Rains, A. D., et al. 2021, *MNRAS*, 507, 2684, doi: [10.1093/mnras/stab2304](https://doi.org/10.1093/mnras/stab2304)
- Chen, B. Q., Huang, Y., Yuan, H. B., et al. 2019, *MNRAS*, 483, 4277, doi: [10.1093/mnras/sty3341](https://doi.org/10.1093/mnras/sty3341)
- El-Badry, K., Rix, H.-W., & Heintz, T. M. 2021, *MNRAS*, 506, 2269, doi: [10.1093/mnras/stab323](https://doi.org/10.1093/mnras/stab323)
- Gaia Collaboration, Antoja, T., McMillan, P. J., et al. 2021, *A&A*, 649, A8, doi: [10.1051/0004-6361/202039714](https://doi.org/10.1051/0004-6361/202039714)
- García Pérez, A. E., Allende Prieto, C., Holtzman, J. A., et al. 2016, *AJ*, 151, 144, doi: [10.3847/0004-6256/151/6/144](https://doi.org/10.3847/0004-6256/151/6/144)
- Green, G. M., Schlafly, E., Zucker, C., Speagle, J. S., & Finkbeiner, D. 2019, *ApJ*, 887, 93, doi: [10.3847/1538-4357/ab5362](https://doi.org/10.3847/1538-4357/ab5362)
- Huang, Y., Yuan, H., Beers, T. C., & Zhang, H. 2021a, *ApJL*, 910, L5, doi: [10.3847/2041-8213/abe69a](https://doi.org/10.3847/2041-8213/abe69a)
- Huang, Y., Chen, B. Q., Yuan, H. B., et al. 2019, *ApJS*, 243, 7, doi: [10.3847/1538-4365/ab1f72](https://doi.org/10.3847/1538-4365/ab1f72)
- Huang, Y., Beers, T. C., Wolf, C., et al. 2021b, arXiv e-prints, arXiv:2104.14154, <https://arxiv.org/abs/2104.14154>
- Ivezić, Ž., Sesar, B., Jurić, M., et al. 2008, *ApJ*, 684, 287, doi: [10.1086/589678](https://doi.org/10.1086/589678)
- Jönsson, H., Holtzman, J. A., Allende Prieto, C., et al. 2020, *AJ*, 160, 120, doi: [10.3847/1538-3881/aba592](https://doi.org/10.3847/1538-3881/aba592)
- Lee, Y. S., Beers, T. C., Sivarani, T., et al. 2008a, *AJ*, 136, 2022, doi: [10.1088/0004-6256/136/5/2022](https://doi.org/10.1088/0004-6256/136/5/2022)
- . 2008b, *AJ*, 136, 2050, doi: [10.1088/0004-6256/136/5/2050](https://doi.org/10.1088/0004-6256/136/5/2050)
- Lee, Y. S., Beers, T. C., An, D., et al. 2011, *ApJ*, 738, 187, doi: [10.1088/0004-637X/738/2/187](https://doi.org/10.1088/0004-637X/738/2/187)
- Lee, Y. S., Beers, T. C., Masseron, T., et al. 2013, *AJ*, 146, 132, doi: [10.1088/0004-6256/146/5/132](https://doi.org/10.1088/0004-6256/146/5/132)
- Lindgren, L., Bastian, U., Biermann, M., et al. 2021, *A&A*, 649, A4, doi: [10.1051/0004-6361/202039653](https://doi.org/10.1051/0004-6361/202039653)
- Luo, A.-L., Zhao, Y.-H., Zhao, G., et al. 2015, *Research in Astronomy and Astrophysics*, 15, 1095, doi: [10.1088/1674-4527/15/8/002](https://doi.org/10.1088/1674-4527/15/8/002)
- Maíz Apellániz, J., & Weiler, M. 2018, *A&A*, 619, A180, doi: [10.1051/0004-6361/201834051](https://doi.org/10.1051/0004-6361/201834051)
- Majewski, S. R., APOGEE Team, & APOGEE-2 Team. 2016, *Astronomische Nachrichten*, 337, 863, doi: [10.1002/asna.201612387](https://doi.org/10.1002/asna.201612387)
- Niu, Z., Yuan, H., & Liu, J. 2021a, *ApJ*, 909, 48, doi: [10.3847/1538-4357/abdbac](https://doi.org/10.3847/1538-4357/abdbac)
- . 2021b, *ApJL*, 908, L14, doi: [10.3847/2041-8213/abec2](https://doi.org/10.3847/2041-8213/abec2)
- Niu, Z., Yuan, H., Wang, S., & Liu, J. 2021, Binary fractions of G and K dwarf stars based on the Gaia EDR3 and LAMOST DR5: impacts of the chemical abundances. <https://arxiv.org/abs/2109.04031>
- Onken, C. A., Wolf, C., Bessell, M. S., et al. 2019, *PASA*, 36, e033, doi: [10.1017/pasa.2019.27](https://doi.org/10.1017/pasa.2019.27)
- Peng, X., Du, C., Wu, Z., Ma, J., & Zhou, X. 2013, *Monthly Notices of the Royal Astronomical Society*, 434, 3165, doi: [10.1093/mnras/stt1232](https://doi.org/10.1093/mnras/stt1232)
- Ren, J. J., Raddi, R., Rebassa-Mansergas, A., et al. 2020, *ApJ*, 905, 38, doi: [10.3847/1538-4357/abc017](https://doi.org/10.3847/1538-4357/abc017)
- Riello, M., De Angeli, F., Evans, D. W., et al. 2021, *A&A*, 649, A3, doi: [10.1051/0004-6361/202039587](https://doi.org/10.1051/0004-6361/202039587)
- Ruiz-Lara, T., Gallart, C., Bernard, E. J., & Cassisi, S. 2020, *Nature Astronomy*, 4, 965, doi: [10.1038/s41550-020-1097-0](https://doi.org/10.1038/s41550-020-1097-0)
- Ruoyi, Z., & Haibo, Y. 2020, *ApJL*, 905, L20, doi: [10.3847/2041-8213/abcccc4](https://doi.org/10.3847/2041-8213/abcccc4)
- Schlafly, E. F., & Finkbeiner, D. P. 2011, *ApJ*, 737, 103, doi: [10.1088/0004-637X/737/2/103](https://doi.org/10.1088/0004-637X/737/2/103)
- Schlegel, D. J., Finkbeiner, D. P., & Davis, M. 1998, *ApJ*, 500, 525, doi: [10.1086/305772](https://doi.org/10.1086/305772)
- Starkenburg, E., Martin, N., Youakim, K., et al. 2017, *MNRAS*, 471, 2587, doi: [10.1093/mnras/stx1068](https://doi.org/10.1093/mnras/stx1068)
- Steinmetz, M., Zwitter, T., Siebert, A., et al. 2006, *AJ*, 132, 1645, doi: [10.1086/506564](https://doi.org/10.1086/506564)
- Weiler, M. 2018, *A&A*, 617, A138, doi: [10.1051/0004-6361/201833462](https://doi.org/10.1051/0004-6361/201833462)
- Whitten, D. D., Placco, V. M., Beers, T. C., et al. 2019, *A&A*, 622, A182, doi: [10.1051/0004-6361/201833368](https://doi.org/10.1051/0004-6361/201833368)
- . 2021, *ApJ*, 912, 147, doi: [10.3847/1538-4357/abee7e](https://doi.org/10.3847/1538-4357/abee7e)
- Wolf, C., Onken, C. A., Luvaul, L. C., et al. 2018, *PASA*, 35, e010, doi: [10.1017/pasa.2018.5](https://doi.org/10.1017/pasa.2018.5)
- Wright, R. J., Lagos, C. d. P., Power, C., & Correa, C. A. 2021, *MNRAS*, 504, 5702, doi: [10.1093/mnras/stab1057](https://doi.org/10.1093/mnras/stab1057)
- Wu, Y., Luo, A. L., Li, H.-N., et al. 2011, *Research in Astronomy and Astrophysics*, 11, 924, doi: [10.1088/1674-4527/11/8/006](https://doi.org/10.1088/1674-4527/11/8/006)
- Xiang, M., Ting, Y.-S., Rix, H.-W., et al. 2019, *ApJS*, 245, 34, doi: [10.3847/1538-4365/ab5364](https://doi.org/10.3847/1538-4365/ab5364)
- Yang, L., Yuan, H., Zhang, R., et al. 2021, *ApJL*, 908, L24, doi: [10.3847/2041-8213/abdbae](https://doi.org/10.3847/2041-8213/abdbae)
- Yanny, B., Rockosi, C., Newberg, H. J., et al. 2009, *AJ*, 137, 4377, doi: [10.1088/0004-6256/137/5/4377](https://doi.org/10.1088/0004-6256/137/5/4377)
- York, D. G., Adelman, J., John E. Anderson, J., et al. 2000, *The Astronomical Journal*, 120, 1579, doi: [10.1086/301513](https://doi.org/10.1086/301513)
- Yuan, H., Liu, X., Xiang, M., Huang, Y., & Chen, B. 2015a, *ApJ*, 799, 134, doi: [10.1088/0004-637X/799/2/134](https://doi.org/10.1088/0004-637X/799/2/134)
- . 2015b, *ApJ*, 803, 13, doi: [10.1088/0004-637X/803/1/13](https://doi.org/10.1088/0004-637X/803/1/13)

Yuan, H., Liu, X., Xiang, M., et al. 2015c, ApJ, 799, 135,
doi: [10.1088/0004-637X/799/2/135](https://doi.org/10.1088/0004-637X/799/2/135)
—. 2015d, ApJ, 799, 133,
doi: [10.1088/0004-637X/799/2/133](https://doi.org/10.1088/0004-637X/799/2/133)
Yuan, H. B., Liu, X. W., & Xiang, M. S. 2013, MNRAS,
430, 2188, doi: [10.1093/mnras/stt039](https://doi.org/10.1093/mnras/stt039)

Zhang, R., Yuan, H., Liu, X., et al. 2021, arXiv e-prints,
arXiv:2109.06390. <https://arxiv.org/abs/2109.06390>